Hierarchically Interlaced 2D Copper Iodide/MXene Composite for High Thermoelectric Performance

*Vaithinathan Karthikeyan, Vaskuri C. S. Theja, Maria Merlyne De Souza, Roy Vellaisamy**

Author name and Affiliation details:
Dr. Vaithinathan Karthikeyan, Vaskuri C. S. Theja
Department of Materials Science and Engineering
City University of Hong Kong
Kowloon Tong, Hong Kong

Prof. Maria Merlyne De Souza
Department of Electronic and Electrical Engineering
University of Sheffield
Sheffield, S3 7HQ, United Kingdom

Prof. Roy Vellaisamy
James Watt School of Engineering
University of Glasgow
Glasgow G12 8QQ, United Kingdom
Email: Roy.Vellaisamy@glasgow.ac.uk

Keywords: *Copper Iodide, MXene, Layered Hierarchy, Nanoinclusion, Thermoelectrics*

Abstract: Hierarchical layered architecture in thermoelectric materials works as an ad hoc methodology for strengthening the unique inherent properties. Here, we demonstrate an excellent thermoelectric behavior in novel 2D copper iodide nanoflakes by compositing with Ti_3C_2 MXene nanoinclusions. The interlaced architecture of CuI/Ti_3C_2 composite lifts the electrical conductivity over two orders by efficient charge transport mechanisms. The thermal conductivity of CuI/Ti_3C_2 composite are reduced by drastic suppression of mid-and high-frequency phonons by interfacial energy barrier scattering. Our structural engineering approach yields a massive power factor of 225 μW m^{-1} K^{-2} and a figure of merit value of 0.48 in CuI/5 vol.% Ti_3C_2 composite. We establish a straightforward approach of tuning the figure of merit in earth-abundant, non-toxic thermoelectric materials to develop future sustainable energy sources.

TOC Figure

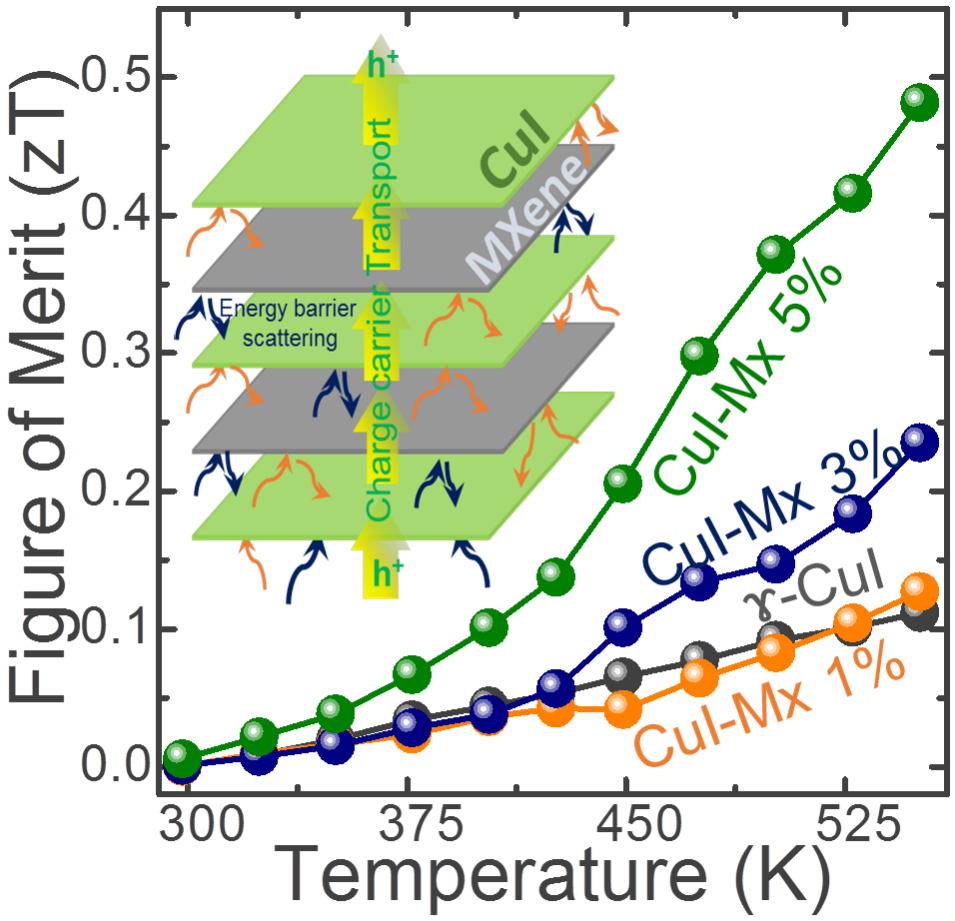

Short Summary

Layered 2D thermoelectric materials are known for their exceptional electrical and thermal properties. Hierarchical structuring of these novel 2D materials enhances the thermoelectric properties of by steadily tuning the electron and phonon transport characteristics in the material. Here we demonstrate the phenomenon of interfacial energy barrier scattering in hierarchically interlaced structure of Copper Iodide with Mxene for enhanced thermoelectric performance.

Environment-friendly and sustainable semiconducting materials are needed due to their massive use in renewable energy generation devices/systems[1,2]. The conventional semiconducting materials for thermoelectric energy conversion primarily are metal chalcogenide (S, Se, Te) compounds as they demonstrate the "electron-crystal, phonon-glass" model[3,4]. Though organic semiconducting materials demonstrate good thermoelectric properties, they are not comparable with power conversion levels and reliability of inorganic compounds at room temperature[5]. Earth-abundant Copper Iodide (CuI) is a p-type semiconducting material with a defect tunable bandgap of 0.9-1.9 eV and is known for its excellent hole-transport property[6–8]. Thermoelectric power conversion in copper iodide thin film and bulk materials are being explored for their transparent and high-hole mobility nature [9–11]. These advanced properties of copper iodide are attributed to the light holes with an effective mass of $0.3m_0$ and zinc-blende type structure[12]. Copper iodide thin film holds the largest figure of merit for transparent thermoelectric thin films with 0.22[13]. Facile and easy synthesis and fabrication of copper iodide materials make them practically ideal for the thermoelectric power conversion process. Though the material experiences low electrical conductivity, its massive Seebeck coefficient of 600 $\mu V\ K^{-1}$ at room temperature reflects the potential power factor of $10^{-4}\ W\ m^{-1}\ K^{-2}$. In recent studies with copper iodide, various simple fabrication routes using both solution process and solid-state synthesis like solid/vapour iodization process[14], pulsed laser deposition[11,15], SILAR process[14], and thermal evaporation[6] were experimented. Irrespective of the synthesis process, the binary copper iodide demonstrates excellent thermal stability in the medium temperature range of 300 - 573 K[16]. To boost the thermoelectrical properties of CuI equivalent to that of the conventional bismuth telluride materials, their electrical conductivity needs to be tuned to the level of 10^2-10^3 S/m. In this aspect, adding secondary semi-conductive nanoinclusion into the matrix of the host can efficiently enhance the

carrier density and additionally scatter phonons via energy barrier scattering[17]. The synergistic effect of nanoinclusion over the carrier and phonon transport in the host matrix has been well demonstrated in the conventional bismuth telluride matrix[18]. Moreover, it is important to prefer nanoinclusions of low dimension type for a larger phase boundary leading to effective to effective transport channeling of the charge carriers and in turn enhance the thermopower[19,20]. Also, thermal conductivity of composites are persistently low as because the bonding and vibrational spectra of the host matrix and nanoinclusion are totally different which creates an anharmonicity[21,22]. Particularly, layered low dimensional thermoelectric materials exhibit strong in-plane bonding, weak out-of-plane bonding featuring bond heterogeneity and their weak interlayer interaction eases the quantum confinement effect for efficient charge carrier transport in the material[23].

Here we report on the boosted thermoelectric properties of solution-processed 2D flakes of γ-CuI bulk material via nano inclusions of layered Ti_3C_2 MXene. We introduce the facile synthesis of γ-CuI nanoflakes and interlaced with Ti_3C_2 secondary phase for the first time. MXenes exhibits metallic transport behaviour and holds equivalent band alignment with CuI, which will support the increase in the power factor of the CuI/Ti_3C_2 composite[24–26]. We demonstrate the proportional increase in the electrical properties of CuI by increasing the volume percentages of Ti_3C_2 in the matrix. The interlaced structure of CuI nanoflakes and MXene nanoinclusions in the matrix helps to significantly rise in power factor and decrease in thermal conductivity, which produces a practically large figure of merit[27,28]. In this work, we focus on developing non-toxic and eco-friendly copper iodide material with MXene interlacing for practical thermoelectric applications.

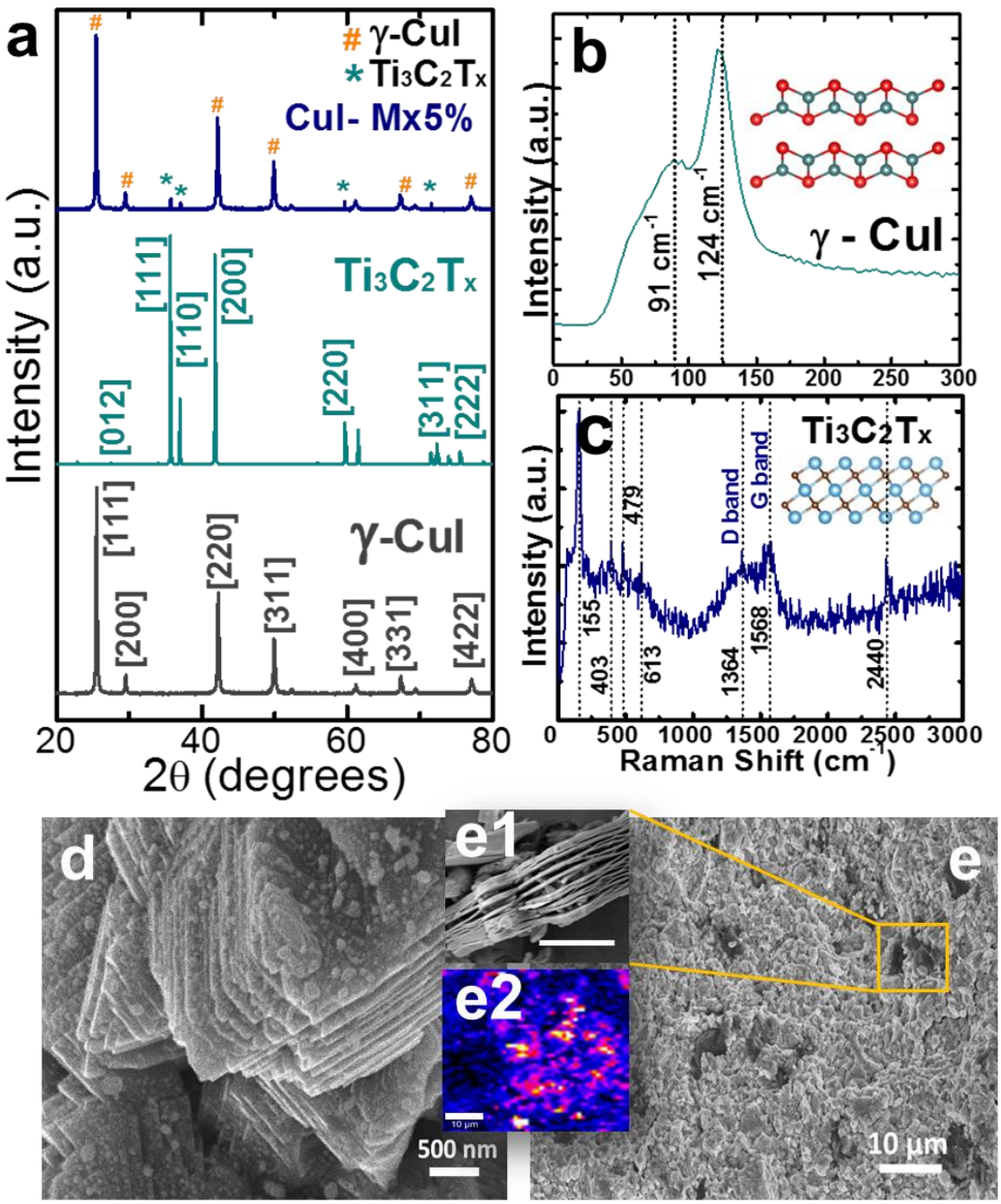

Figure 1(a) *XRD pattern comparison for γ -CuI, Ti_3C_2, and hot-pressed CuI-Mx5% samples* ***(b)*** *and* ***(c)*** *Raman analysis for CuI-Mx5% representing the characteristic peaks for CuI and Ti_3C_2 respectively* ***(d)*** *FESEM image showing layered stacking of CuI nanoflakes in the hot-pressed sample* ***(e)*** *FESEM image for CuI-Mx5% showing the interlacing of Ti_3C_2. Inset images* ***(e1)*** *and* ***(e2)*** *represent the Ti_3C_2 present and Raman mapping of the distribution of Ti_3C_2 in CuI-Mx5%, respectively.*

Figure 1 shows the structural characterization of the fabricated CuI/Ti_3C_2 composite where the X-ray diffraction pattern matches with the cubic γ-phase of CuI and the standard pattern of JCPDS card no: 06-0246 with high crystallinity [16]. The XRD pattern of the sample with CuI/5% Ti_3C_2 MXene interlacing exhibits the characteristic peaks [111], [110], and [220] of Ti_3C_2. Raman spectrum of the corresponding sample depicts the characteristic transverse-optical mode of CuI at 91 cm^{-1} and 124 cm^{-1} and the Ti_3C_2 characteristic D and G band at 1364 cm^{-1} and 1568 cm^{-1} respectively [9,24]. Figure 1d shows the layered stacking of pristine copper iodide nanoflakes in the hot-pressed sample, this layered material morphology is particularly preferred for exceptional carrier transport satisfying the electron-crystal model.

The 2D layered growth of CuI nanoflakes along the [111] plane resembles the growth pattern of transition metal dichalcogenides typically representing triangular shapes with the size of 1-3 μm[29]. FESEM image in figure 1e shows the uniform distribution of 5 vol.%Ti_3C_2 MXene in CuI matrix and demonstrates a high-density nature of the pelletized samples without any observation of porous structures. The inset image figure 1e1 shows the layered structure of MXene interlaced in the CuI matrix. Inset image figure 1e2 shows the Raman mapping of the CuI/Ti_3C_2 matrix, which explains the distribution uniformity level of interlaced Ti_3C_2. Micro/nanostructure characteristics of the composite are distinctly observed from the back scattered electron SEM analysis as shown in supporting information figure S1. Further to understand the possible band structure of CuI and electronic density of states of CuI and Ti_3C_2 matrix, we performed the DFT-VASP calculation as shown in figure 2[30,31]. The addition of the secondary phase can add cause alterations in the effective mass of the matrix band structure.

Table 1 *Thermoelectric properties of CuI matrix with different Ti_3C_2 inclusion vol.% at room temperature.*

MXene (Vol.%)	Density (g/cm^3)	Seebeck Coefficient (μV/K)	Electrical Conductivity (S/cm)	Carrier Concentration ($x10^{19}$ cm^{-3})	Effective Mass (m^*/m_0)	Effective density of states ($x10^{18}$ cm^{-3})
0	5.32	254	0.50	0.03	0.02	0.11
1	5.31	104	1.56	0.16	0.09	0.70
3	5.28	90	4.72	1.13	0.48	8.57
5	5.27	70	21.79	8.4	2.02	73.68

Figures 2a and 2b illustrate the effective charge transfer channeling and interfacial energy barrier scattering induced in the interlaced architecture of CuI/Ti_3C_2 composite. According to energy scattering theory, energy-dependent charge carrier scattering or channeling occurs at the interface barrier of secondary phase nanoinclusions allowing only the charges with higher energy only can penetrate through the interface. The level of the energy barrier depends on the choice of the nanoinclusion, which significantly influences the electrical and Seebeck coefficient of the host matrix. Figure 2b shows the energy barrier difference between CuI and Ti_3C_2 band alignments, causing strong phonon scattering decreasing thermal conductivity[18,27]. Figure 2c shows the band structure plot for γ-CuI having a direct bandgap of 1.9 eV. The thermoelectric potential of a material principally depends on its electronic band structure located near the valence band edge. The bands at the valence band edge correspond to the effective mass, which determines the Seebeck coefficient of the material[30]. The presence of less dispersive bands at the valence band edge of CuI demonstrates lower effective mass and electrical conductivity. Hence, altering the CuI

matrix's effective mass with conductive nanoinclusions will significantly produce large power factor in the composite.

Figure 2d shows the overlapping view of the electronic density of states of the CuI and Ti_3C_2 where it is seen that the states of Ti_3C_2 fill the bandgap edges of the CuI. The strong conductive nature of the Ti_3C_2 electronic band structure promotes instant charge transfer channeling between the interfaces leading to an increase in electrical conductivity. Moreover, the associated phonon energy with the phonons is scattered during the band transition in the matrix via the energy barrier scattering, thereby achieving low thermal conductivity in the CuI/Ti_3C_2 composite. With this theoretical understanding, thermoelectric properties in the Ti_3C_2 interlaced CuI matrix were examined, as shown in figure 3. Hot-pressed CuI nanoflakes morphology demonstrates massive thermopower when compared to the previously reported CuI nanoparticles. At room temperature, the thermopower (S) for the pristine CuI nanoflakes sample demonstrates 250 μV/K and with a maximum of 760 μV/K in the mid-range at 425 K. This large thermopower in CuI arise from the dominant donor type defects, which are compensated by the hole density[32].

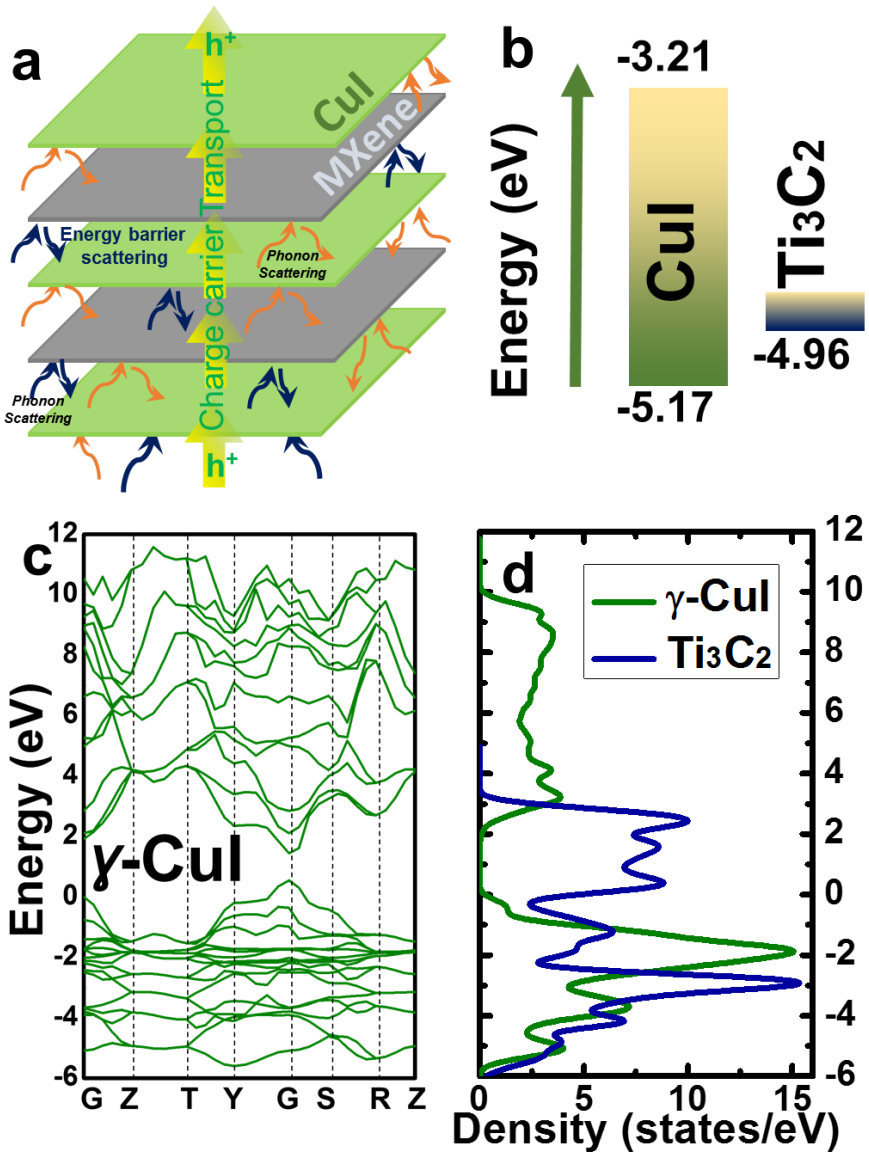

Figure 2 (a) *and* ***(b)*** *illustrates the effect of interlaced architecture for energy barrier scattering and the work function difference between CuI and* Ti_3C_2 *respectively. (c) Electronic band structure of CuI matrix by DFT-VASP calculations* ***(d)*** *Overlapped view of electronic density of states for the CuI and* Ti_3C_2*.*

For the Ti_3C_2 interlaced CuI samples, thermopower decreases with an increase in the nanoinclusion percentage; however, they demonstrate a steady level throughout the temperature range. A minimum value of 233 μV/K is recorded for CuI with 5 vol.% Ti_3C_2 at 550 K, this level of high thermopower efficiently balances the lower electrical conductivity for realizing high power factor

values. The observed decrease in the Seebeck coefficient is harmonized by the increasing scattering parameter in CuI/Ti_3C_2 composite, which principally is attributed to the energy barrier scattering. Naturally, the pristine CuI nanoparticles depict an electrical conductivity (σ) of 10^{-2} S/cm, whereas the CuI nanoflakes show improved electrical performance. High-quality Ti_3C_2 MXene defined layered architecture possesses electrical conductivity of 10^4 S/cm, which, when interlaced within the CuI nanoflakes will uplift the electrical conductivity of the host matrix[17,33]. This phenomenon was observed in the temperature-dependent electrical conductivity measurement of the CuI/Ti_3C_2 composite. The equivalent work function facilitates hole injection from the CuI and Ti_3C_2 matrix, which raises the composite's electrical conductivity.

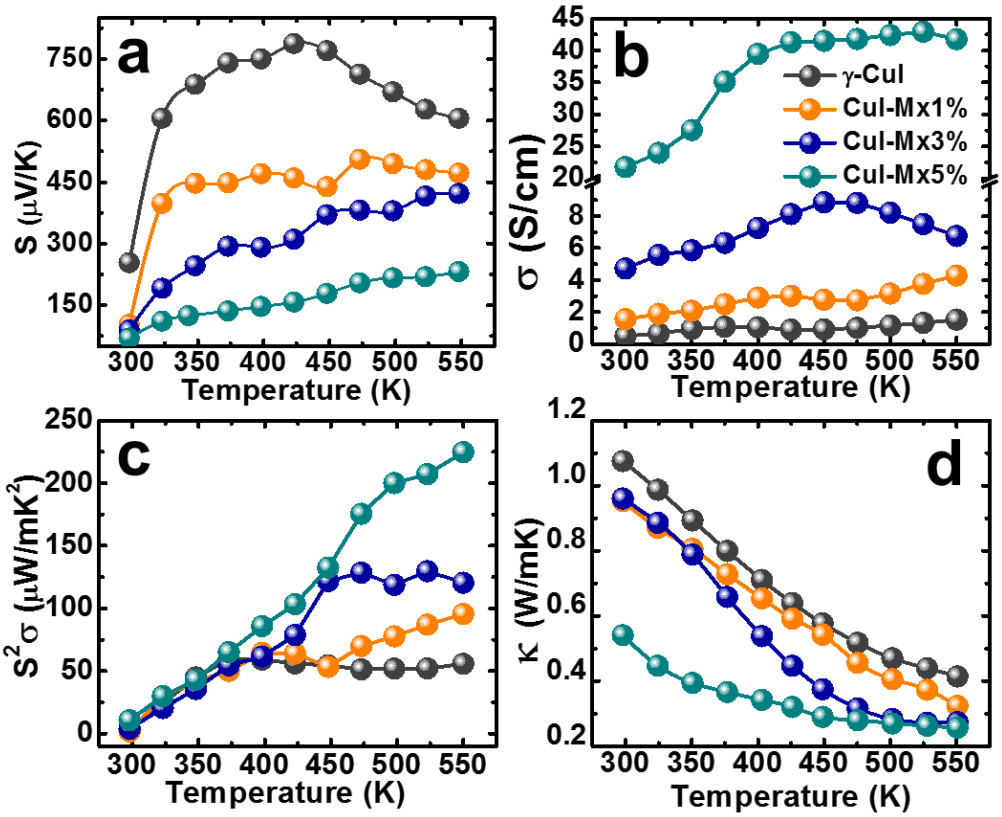

Figure 3 *Temperature-dependent thermoelectric properties of CuI/Ti_3C_2* ***(a)*** *Seebeck Coefficient* ***(b)*** *electrical conductivity* ***(c)*** *Power Factor and* ***(d)*** *Thermal conductivity with respect to the Ti_3C_2 nanoinclusion vol. % respectively.*

As shown in figure 3b, the electrical conductivity value rises considerably with the inclusion % of Ti_3C_2. A maximum σ of 42 S/cm was demonstrated for 5 vol% Ti_3C_2, which significantly promotes the rise in their corresponding power factor. Thus, via Ti_3C_2 nanoinclusion and the interlaced architecture of CuI/Ti_3C_2 composite, we achieved a two-order rise in the electrical conductivity, making CuI undoubtedly a potential thermoelectric material for real-time heat energy conversion applications[11,34]. Ti_3C_2 nanoinclusion balanced S and σ demonstrates over four-fold increase in the power factor from 55 μW/mK^2 in pristine to 225 μW/mK^2 in 5 vol.% Ti_3C_2 at 550 K. This massive rise in the power factor of the CuI/Ti_3C_2 composite solely attributed to the interlacing morphology and densification process utilized in our experiment. This level of massive power factor makes CuI a suitable candidate to replace the performance of commercial Bi_2Te_3 both economically and ecofriendly aspects. Synergistically, the 2D layered nanoinclusion in the host CuI matrix also contributed to the scattering of phonon transport via the energy barrier scattering. During the charge carrier transfer between the CuI and Ti_3C_2 happens the mid and high-frequency phonons are effectively scattered in the matrix. This effect is physically observed from the temperature-dependent thermal conductivity shown in figure 3d. With low vol.% of Ti_3C_2, the thermal conductivity increases owing to the electronic contribution part of thermal conductivity, whereas for the concentration of 5 vol.%, the thermal conductivity drastically falls in the lower and mid-temperature range signifying the scattering of mid and high-frequency phonons by the interlaced CuI/Ti_3C_2 composite[35]. The repeatability of the thermoelectric performance were tested multiple times and the deviations are less than 5%, which demonstrates the stability of the material and measurements as shown in supporting information figure S2 with error bars. Detailed study on thermal stability and specific heat capacity of the CuI/MXene composite are presented in

figure S3, where the thermal stability of the composites is enhanced with increasing ratio of MXene nanoinclusion.

Predominantly to outline the mechanism involved in boosting the thermoelectric performance of the nanoinclusion based CuI/Ti_3C_2 composite, the Pisarenko relation and carrier dynamics are shown in Figures 4a and 4b. Seebeck coefficient for a degenerate semiconductor are given from the single parabolic band approximation model as below:

$$S = \frac{8\pi^2 k_B^2 T}{3eh^2} m^* \left(\frac{\pi}{3p}\right)^{2/3}$$

where S is the Seebeck coefficient, m^* is the effective mass, e is the electron charge, h is plank constant, p is the hole density, k_B is the Boltzmann constant and T is absolute temperature, respectively. γ-CuI has an effective mass of $0.30m_0$ for light holes and $2.14m_0$ for heavy holes, which report low carrier density and mobility[36]. In our case, the increase in effective mass and effective density of states causes the scattering of charge carriers with low energy which restrains the drastic decrease in the Seebeck coefficient as shown in Table 1. This existence is observed from the Pisarenko relation calculated from the above relation where the Seebeck and the carrier density rise follows the single parabolic band model indicating increasing band curvature and mass. Figure 4b shows the increasing carrier density with respect to increasing Ti_3C_2 nanoinclusion vol.% and decreased carrier mobility which is universally experienced in most nanoinclusion-based experimental cases[18]. However, in this experimental study, the 2D CuI nanoflakes and Ti_3C_2 layers interlacing structure provides significant enhancement carrier transport through the heterojunction interface by hole injection process. Further to evidence the established superior charge carrier transport between the CuI and Ti_3C_2 interface, we performed the impedance spectroscopy analysis using electrochemical workstation on the hot-press densified CuI/Ti_3C_2

matrix. Figure 4c compares the impedance curves of the pristine CuI with the interlaced structure of CuI/Ti_3C_2 composite. The charge transport in the matrix is enriched with the inclusion of Ti_3C_2 in the host CuI matrix by decreasing interface resistance[18].

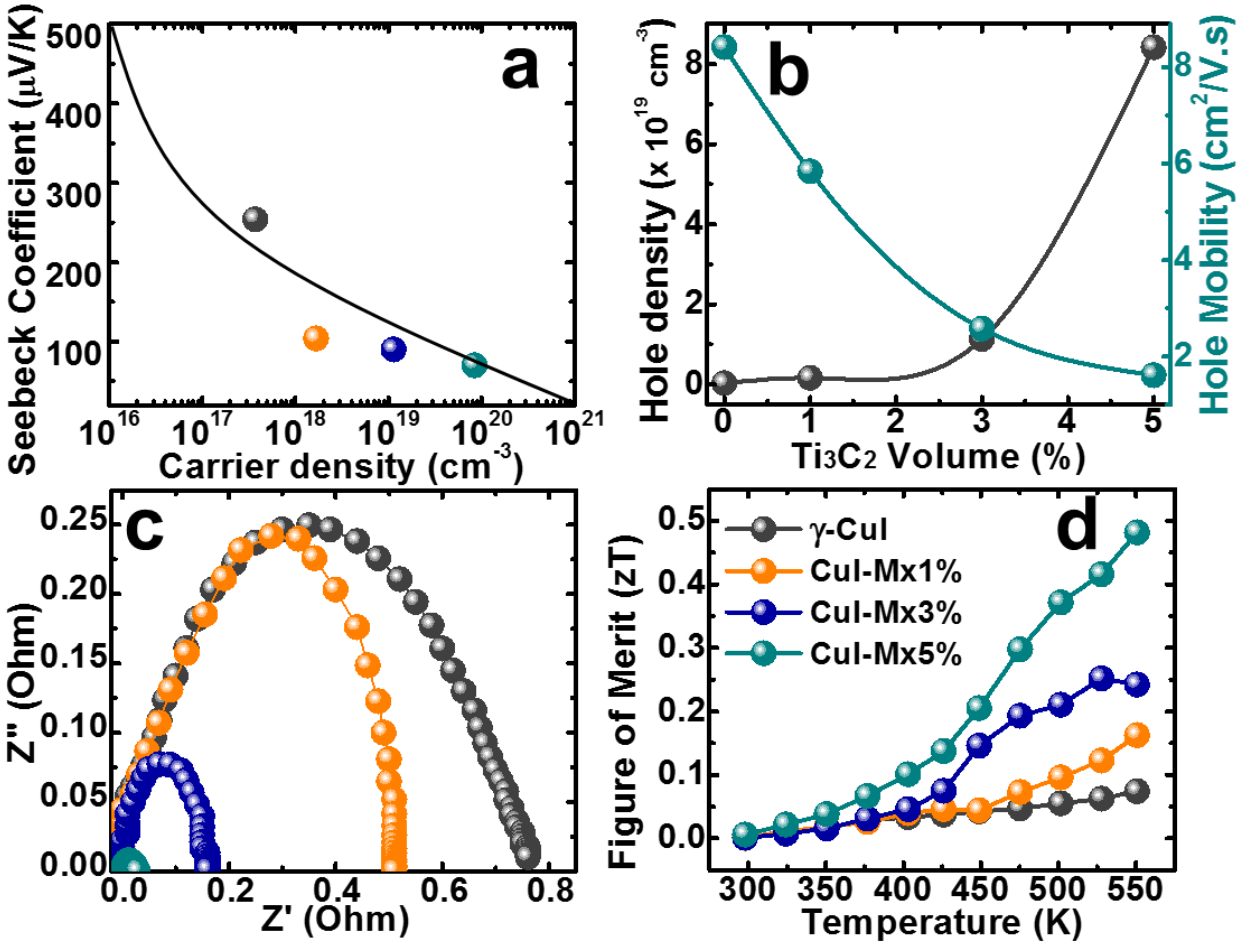

Figure 4 (a) *Pisarenko plot showing Seebeck coefficient versus carrier density at room temperature* ***(b)*** *Carrier dynamics of CuI/Ti_3C_2 composite showing the change in hole concentration and mobility* ***(c)*** *Change in Impedance curves for the CuI/Ti_3C_2 composite samples* ***(d)*** *Temperature-dependent figure of merit values for different vol.% of CuI/Ti_3C_2 composite samples.*

As a result of the intertwined carrier transport and filtered scattering of phonons causes a consequential increase in the figure of merit of CuI/Ti_3C_2 composite. Figure 4d demonstrates the

progressive rise of the figure of merit with Ti_3C_2 inclusions. Though the pristine CuI exhibits poor electrical and high thermal conductivity, the intrinsic massive thermopower consistency over the temperature range supports in demonstrating a figure of merit of 0.11 at 550 K. For the samples with rising Ti_3C_2 vol.%, the figure of merit benefits to shooting owing to their corresponding rise in electrical conductivity. A maximum figure of merit of 0.48 is commendably recorded for 5 vol.% Ti_3C_2 nanoinclusion in the CuI matrix. This proves that the capacity of CuI to be a potential thermoelectric material with an effective structure and interfacial engineering for the depiction of an advanced charge transfer path in the material. For samples over 5 vol.% of Ti_3C_2, the sample demonstrates a strong tendency of agglomeration, which is common in the ultrathin structure of 2D materials beyond certain the domination of metallic nature in the samples.

In conclusion, we established a facile, straightforward method for the controlled synthesis of CuI nanoflakes. Layered structures of Ti_3C_2 MXene are interlaced with CuI nanoflakes as nanoinclusions in different vol.% for superior charge carrier transport. We demonstrate the band alignment and modifications in the total density of states through our detailed theoretical calculations. The interlaced design of the matrix exclusively supports enabling interfacial energy barrier scattering of mid and high-frequency phonons, thereby achieving low thermal conductivity. This strategic approach allows tuning of thermoelectric figures of merit for meeting the application requirements. Overall, this demonstration of engineering figure of merit in easily processable earth-abundant thermoelectric materials can lead to future eco-friendly energy sources. Though many natural intergrowth structures exist with ultralow lattice thermal conductivity, their unfavorable charge transport properties cause by weak interlayer bonding degrades the power factor of the material. As layered interfaces are well explored for strong phonon scattering process,

these novel class layered materials should be further explored with interlacing hierarchy for efficient thermoelectric power conversion process.

Experimental Section

2D Copper Iodide nanoflakes are synthesized by solution process using Copper powder (Goodfellow, 99.99%) and Iodine pellets (Fluka, 99.99%). 1 M iodine solution was prepared using ethanol where the copper powder is mixed and stirred continuously for 5 hours at 80^{o}C. The resultant product in the solution is collected then washed in ethanol and dried in a vacuum. For the process of Ti_3C_2 interlacing or nanoinclusion, the dried CuI powder is dispersed in ethanol with specific vol.% of Ti_3C_2 MXene and ultra-sonicated using probe sonication (Scientz-iid ultrasonic homogenizer). The dried interlaced CuI/Ti_3C_2 composite is hot pressing at 550 K under 50 MPa for the high densification process. The density of the pellets is measure by the Archimedes method where it retains 98% of the theoretical density of CuI. The Raman spectra are recorded using an excitation cobalt DPL laser wavelength of 532 nm in WITec RAMAN alpha 300R equipment to understand the phase formations using molecular bonding-related vibrational intensities and carbon G-band regional Raman mapping. The carrier concentration and carrier mobility are calculated using the HMS-3000 Hall measurement system using the van-der-paaw method. The Seebeck coefficient and electrical conductivity are measured by standard four-probe direct current measurement using Netzsch SBA 458 Nemesis and the thermal conductivity is measured by a light flash method using Netzsch LFA 468 in the temperature range between 300-550 K. Thermal properties like thermal stability, heat flow was measured using Simultaneous Thermal Analyzer (STA) of model PerkinElmer STA6000 up to 1000K. Impedance analyses were performed using the CHI instruments in the frequency range of 10^{-3} -10^{2} Hz. Theoretical calculation for the electronic band structure and density of states were performed using the density

functional theory with the help of Vienna ab initio simulation package(VASP). Before the calculation of band structure and density of states the crystal structure of CuI and Ti_3C_2 are completely relaxed with conjugated-gradient algorithm. Monkhorst-Pack k-point of 6 x 6 x 6 with energy cut-off 400 eV were used.

Acknowledgement

We acknowledge grants from the Research Grants Council of Hong Kong Special Administrative Region Project no: T42-103/16N

Conflict of Interest

The authors declare no conflict of interest.

Reference

[1] O. Caballero-Calero, J. R. Ares, M. Martín-González, *Adv. Sustain. Syst.* **2021**, 2100095.

[2] X. Hei, S. J. Teat, W. Liu, J. Li, *J. Mater. Chem. C* **2020**, *8*, 16790.

[3] Y. Yu, M. Cagnoni, O. Cojocaru-Mirédin, M. Wuttig, *Adv. Funct. Mater.* **2020**, *30*, 1904862.

[4] Y. Pei, H. Wang, G. J. Snyder, *Adv. Mater.* **2012**, *24*, 6125.

[5] M. Lindorf, K. A. Mazzio, J. Pflaum, K. Nielsch, W. Brütting, M. Albrecht, *J. Mater. Chem. A* **2020**, *8*, 7495.

[6] C. Yang, D. Souchay, M. Kneiß, M. Bogner, H. M. Wei, M. Lorenz, O. Oeckler, G. Benstetter, Y. Q. Fu, M. Grundmann, *Nat. Commun.* **2017**, *8*, 4.

[7] N. Yamada, R. Ino, Y. Ninomiya, *Chem. Mater.* **2016**, *28*, 4971.

[8] Y. Zheng, T. J. Slade, L. Hu, X. Y. Tan, Y. Luo, Z.-Z. Luo, J. Xu, Q. Yan, M. G. Kanatzidis, *Chem. Soc. Rev.* **2021**, *50*, 9022.

[9] P. P. Murmu, V. Karthik, S. V Chong, S. Rubanov, Z. Liu, T. Mori, J. Yi, J. Kennedy, *Emergent Mater.* **2021**, *4*, 761.

[10] J. Coroa, B. M. Morais Faustino, A. Marques, C. Bianchi, T. Koskinen, T. Juntunen, I. Tittonen, I. Ferreira, *RSC Adv.* **2019**, *9*, 35384.

[11] P. Storm, M. S. Bar, S. Selle, H. von Wenckstern, M. Grundmann, M. Lorenz, *Phys. status solidi – Rapid Res. Lett.* 2015, *8*, 2100214.

[12] W. Yu, G. Benndorf, Y. Jiang, K. Jiang, C. Yang, M. Lorenz, M. Grundmann, *Phys. Status Solidi - Rapid Res. Lett.* **2021**, *15*, 1.

[13] B. M. Morais Faustino, D. Gomes, J. Faria, T. Juntunen, G. Gaspar, C. Bianchi, A. Almeida, A. Marques, I. Tittonen, I. Ferreira, *Sci. Rep.* **2018**, *8*, 6867.

[14] N. P. Klochko, V. A. Barbash, K. S. Klepikova, V. R. Kopach, I. I. Tyukhov, O. V. Yashchenko, D. O. Zhadan, S. I. Petrushenko, S. V. Dukarov, V. M. Sukhov, A. L. Khrypunova, *Sol. Energy* **2020**, *212*, 231.

[15] P. H. Le, C. W. Luo, *Appl. Laser Ablation - Thin Film Depos. Nanomater. Synth. Surf. Modif.* **2016.**

[16] R. Mulla, M. K. Rabinal, *Energy Technol.* **2018**, *6*, 1178.

[17] T. G. Novak, K. Kim, S. Jeon, *Nanoscale* **2019**, *11*, 19684.

[18] X. Lu, Q. Zhang, J. Liao, H. Chen, Y. Fan, J. Xing, S. Gu, J. Huang, J. Ma, J. Wang, L. Wang, W. Jiang, *Adv. Energy Mater.* **2020**, *10*, 1902986.

[19] Y.-X. Chen, X.-L. Shi, Z.-H. Zheng, F. Li, W.-D. Liu, W.-Y. Chen, X.-R. Li, G.-X. Liang, J.-T. Luo, P. Fan, Z.-G. Chen, *Mater. Today Phys.* **2021**, *16*, 100306.

[20] Y. Xiao, L.-D. Zhao, *Science*, **2020**, *367*, 1196 .

[21] V. Karthikeyan, C. M. Arava, M. Z. Hlaing, B. Chen, C. H. Chan, K.-H. Lam, V. A. L. Roy, *Scr. Mater.* **2020**, *174*, 95.

[22] X.-L. Shi, W.-Y. Chen, T. Zhang, J. Zou, Z.-G. Chen, *Energy Environ. Sci.* **2021**, *14*, 729.

[23] M. Samanta, T. Ghosh, S. Chandra, K. Biswas, *J. Mater. Chem. A* **2020**, *8*, 12226.

[24] G. Lee, Y.-J. Lee, K. Palotás, T. Lee, A. Soon, *J. Phys. Chem. C* **2020**, *124*, 16362.

[25] K. Krupski, M. Moors, T. Kobiela, A. Krupski, *Materials*, **2015**, *6* 2935.

[26] A. Miranda, J. Halim, M. W. Barsoum, A. Lorke, *Appl. Phys. Lett.* **2016**, *108*, 33102.

[27] W. Ding, P. Liu, Z. Bai, Y. Wang, G. Liu, Q. Jiang, F. Jiang, P. Liu, C. Liu, J. Xu, *Adv. Mater. Interfaces* **2020**, *7*, 2001340.

[28] R. Li, L. Zhang, L. Shi, P. Wang, *ACS Nano* **2017**, *11*, 3752.

[29] K. Yao, P. Chen, Z. Zhang, J. Li, R. Ai, H. Ma, B. Zhao, G. Sun, R. Wu, X. Tang, B. Li, J. Hu, X. Duan, X. Duan, *npj 2D Mater. Appl.* **2018**, *2*, 1.

[30] M. K. Yadav, B. Sanyal, *Mater. Res. Express* **2014**, *1*, 015708.

[31] A. N. Enyashin, A. L. Ivanovskii, *J. Phys. Chem. C* **2013**, *117*, 13637.

[32] K. Nishikawa, Y. Takeda, T. Motohiro, *Appl. Phys. Lett.* **2013**, *102*, 33903.

[33] J. Zhou, Z. Lin, H. Ren, X. Duan, I. Shakir, Y. Huang, X. Duan, *Adv. Mater.* **2021**, *33*, 2004557.

[34] J. V. Kennedy, P. P. Murmu, V. Karthik, Z. Liu, V. Jovic, T. Mori, W. L. Yang, K. E.

Smith, *ACS Appl. Energy Mater.* **2020**, *3*, 10037.

[35] Z. Chen, B. Ge, W. Li, S. Lin, J. Shen, Y. Chang, R. Hanus, G. J. Snyder, Y. Pei, *Nat. Commun.* **2017**, *8*, 13828.

[36] J. Wang, J. Li, S.-S. Li, *J. Appl. Phys.* **2011**, *110*, 54907.

Supporting Information

Hierarchically Interlaced 2D Copper Iodide/MXene Composite for High Thermoelectric Performance

*Vaithinathan Karthikeyan, Vaskuri C. S. Theja, Maria Merlyne De Souza, Roy Vellaisamy**

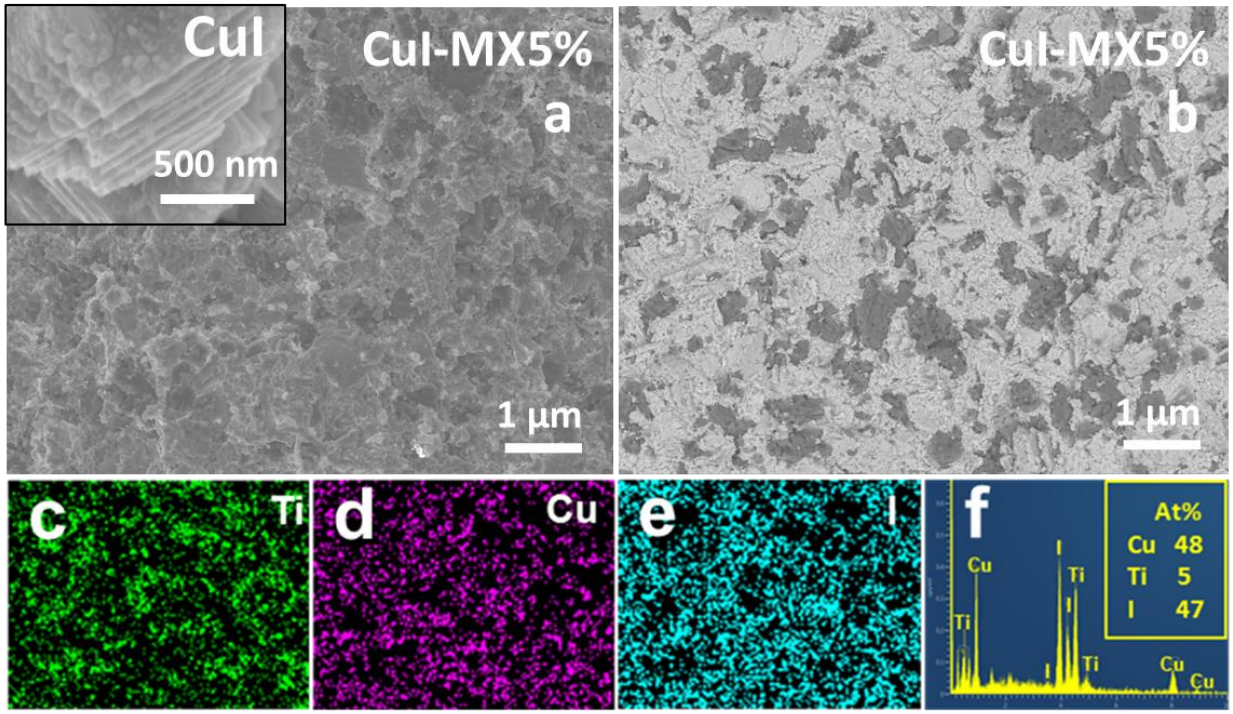

Figure S1 (a) *SEM Image-Secondary electron (Inset: Pristine Nano flakes of CuI)* ***(b)*** *SEM Image-Back scattered electron* ***(c)***, ***(d)***, ***(e)*** *elemental mapping* ***(f)*** *EDAX elemental composition of CuI/5% Mxene composite respectively.*

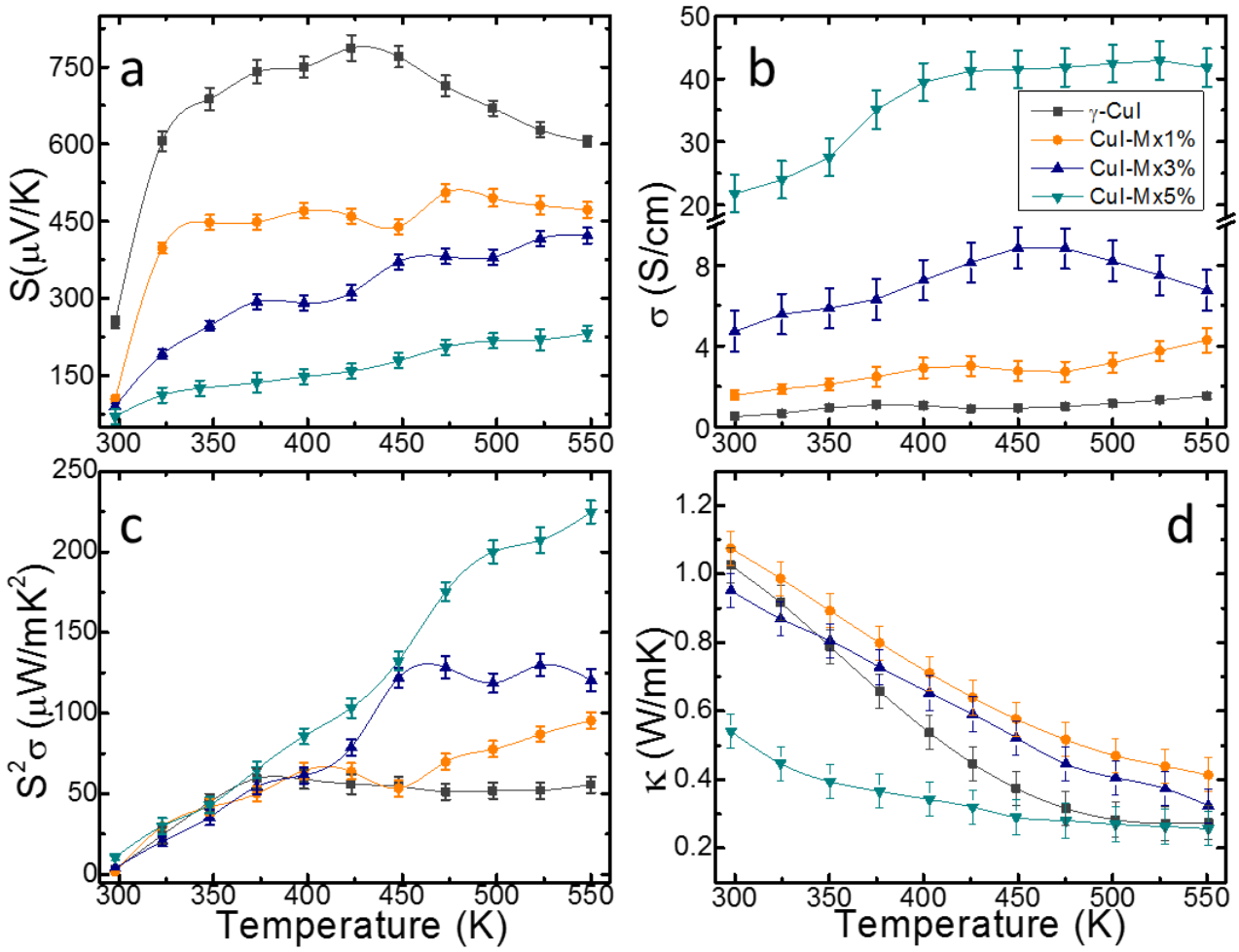

Figure S2 *Repeatability of thermoelectric properties in CuI/MXene with error bars*

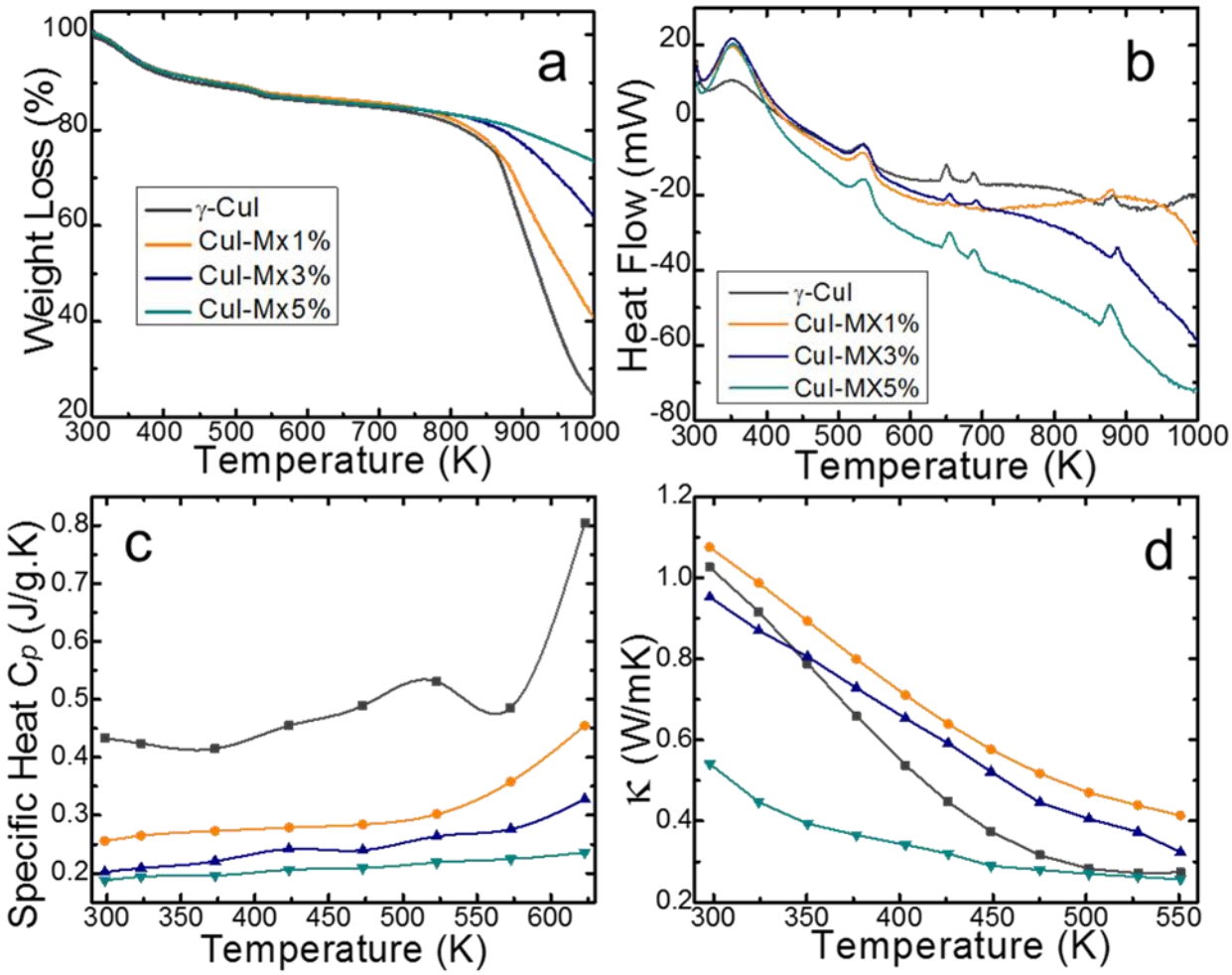

Figure S3 (a) *TGA curve* ***(b)*** *Heat flow* ***(c)*** *specific heat and* ***(d)*** *thermal conductivity of the CuI/Mxene composite*